Hindawi
Geofluids
Volume 2021, Article ID 6671597, 11 pages
https://doi.org/10.1155/2021/6671597

Research Article

Experimental Study on the Effect of Long-Term Water Injection on Micropore Structure of Ultralow Permeability Sandstone Reservoir

Shiyuan Qu,[1] **Hanqiao Jiang**,[1] **Junjian Li**,[1] **Lin Zhao**,[1] **and Changhui Wu**[2]

[1]*State Key Laboratory of Petroleum Resources and Prospecting, China University of Petroleum (Beijing), Beijing 102249, China*
[2]*Research Institute of Shaanxi Yanchang Petroleum (Group) Co. Ltd., Xi'an, Shaanxi 710075, China*

Correspondence should be addressed to Shiyuan Qu; 2016312038@student.cup.edu.cn

Received 1 November 2020; Revised 26 December 2020; Accepted 8 January 2021; Published 2 February 2021

Academic Editor: Shiyuan Zhan

During the long-term waterflooding (LTWF) in oil reservoirs, the formation is subject to permeability reduction as clay release and fine migration. At present, the mechanisms of permeability impairment in both macroscopic and microscopic pore structures in ultralow permeability reservoirs under LTWF are unclear. This statement epitomizes the main objective of this work: to understand how long-term waterflood changes porous structures and thus compromises permeability. The standard core flow experiments in conjunction with a couple of tests consisting of online nuclear magnetic resonance (NMR), high-pressure mercury intrusive penetration (HPMIP), X-ray diffraction (XRD), and scanning electron microscope (SEM) were performed to determine the mineral compositions, macrophysical properties, and micropore structures of two kinds of cores with different natures of pore distribution (i.e., unimodal and bimodal) before and after LTWF in Yan Chang field China. Results showed that the permeability decreased while the porosity increased after the LTWF. With respect to the pore size distribution, the small pores (SPs) decreased and the large pores (LPs) increased for both cores. For the unimodal core, the distribution curve shifted upwards with little change in the radius of the connected pores. For the bimodal core, the curve shifted to the right with an increasing radius of connected pores. With respect to the characteristic parameters, the average pore radius, median pore radius, structural coefficient, and tortuosity increased, while the relative sorting coefficient decreased. The relative changes of the parameters for the unimodal core were much smaller than those for the bimodal core. With respect to the clays, chlorite accounted for a majority proportion of the clays, and its content increased after LTWF. According to these changes, the mechanism of LTWF at different stages was interpreted. At the early stages, the blockage of the released clays occurred in SPs. Some of the middle pores (MPs) and LPs became larger due to the release and some of them became smaller due to the accumulation. At the middle stage, the blockage of SPs weakened. Some flow channels formed by MPs and LPs became dominant flow channels gradually. The effluxes of particles occurred, resulting in a significant increase in porosity. At the late stage, the stable flow channels have formed. The higher response of the bimodal core to LTWF could be attributed to its higher content of chlorite, which was more likely to accumulate. This study clarifies the mechanism of fine-migration-induced formation damage in microscopic pore structures and the migration pattern of clay minerals in ultralow permeability reservoirs. The work provides potential guidance for optimizing waterflood strategies in ultralow permeability reservoirs.

1. Introduction

After natural depletion, water flooding is universally recognized as an effective method to realize an additional production of oil [1–3]. Regarding extralow permeability reservoirs at the middle and later periods of water injection development, however, the sharp rise of injection pressure and difficulty in water injection hinder the expected performance [4–6]. The production cost and irreversible permeability reduction induced by reservoir damage are up to USD 140 billion a year [7]. Therefore, it is necessary to carry out systematic research on the changes of pore throat structure and its

mechanism in the low-permeability reservoir during the LTWF process, to provide a reference for the prevention of reservoir damage.

The influence of LTWF on low-permeability reservoirs has attracted more and more attention recently. With the increase of injected water, the water saturation climbs, and under long-term water erosion, the reservoir physical properties change, especially the porosity and permeability. Li and Xu [8] compared the influence of LTWF between high-permeability and low-permeability reservoirs by water flooding experiment. Results show that the pore connectivity of high-permeability reservoir would be improved after LTWF, while the permeability reduction of low-permeability reservoir would exist due to the throat blockage caused by fine migration. Du et al. [9–11] came to the similar conclusion through various experimental means and field data studies; that is, there would be enhancement in physical property in high-permeability reservoirs, while the damage would occur in low-permeability reservoirs after LTWF. Regarding the problem, scholars have carried out related researches using experiments and field data, but they only studied the damage degree of LTWF to low-permeability cores of different permeability levels, as well as the impact of flooding parameters (e.g., water injection speed) on the degree of damage [12–14]. At present, there is no systematic experimental method to study the reservoir damage dynamics caused by LTWF, and the damage mechanism of low-permeability reservoirs also remains unclear.

The reservoir damage from water flooding is usually associated with fines migration. In fact, the change of formation fluid alters the rock surface charge, which causes particles such as clay to fall off from the rock surface and migrate with the formation fluid. In the process of migration, the particles may undergo physical settlement due to the stagnation of the fluid flow. Eventually, the particles may accumulate in the throat, preventing fluid flow and leading to the loss of permeability. Yu et al. [15] studied the water damage caused by the dispersed migration of kaolinite minerals in Berea sandstone by the core flooding test and found that the critical salinity is only related to the type of cation, but has nothing to do with the type and velocity of the anion. The critical salinity of the divalent cation is very small, and the critical salinity of univalent cation drops with the decrease of hydration ion radius. The critical salinity is the salinity when the permeability ratio of posttreated permeability to primary permeability starts inflecting [16]. Omar et al. [17, 18] further considered that water-sensitive damage was related to the type and content of exchangeable cations in clay minerals. Wilson et al. [19, 20] reviewed the role of single clay minerals in formation damage caused by fine particle migration, and kaolinite and illite (including mixed illite/-montmorillonite) were identified as the main source of particles for migration. However, the role of montmorillonite and chlorite in formation damage still remains unclear. Although the formation damage tests in bottles proved that montmorillonite could expand and form a gelatinous substance under the action of water, which had the potential of causing permeability loss, the molecular simulation tested by Odriozola and Guevara-Rodríguez [21] suggested that such montmorillonite expansion is almost impossible in actual reservoirs. In brief, for low-permeability reservoirs, although the permeability loss caused by long-term water injection has been confirmed in field practice and core flooding experiments, its permeability loss mechanism has not yet been clarified. Hence, on the basis of evaluating the permeability loss degree in the process of water injection, it is necessary to establish new systematic experimental methods to further visualize the dynamic changes of pore structure and clay minerals in the process of water injection, to reveal the permeability loss mechanism.

The original experimental methods used to study the mechanism of reservoir damage mainly include electron microscopy (SEM) [22], X-ray diffraction (XRD) [23], and X-ray fluorescence (XRF) [24]. Although these methods can provide an intuitive and quantitative means to study the dynamic changes of clay minerals in the core, they all need to destroy the samples in the process of analysis, which usually requires lots of experiments to statistically compare the changes of pore structure and clay minerals before and after the formation damage. Due to the strong heterogeneity of the reservoir, many scholars have drawn contradictory conclusions through these research methods [4, 7]. In recent years, the emergence of a large number of advanced research methods can do help for clarifying the oil-water-rock mechanisms at the pore scale. Through the method of core flooding tests coupled with micro-CT scans [25], the dynamic changes of pore structure in the water injection process of sandstone were revealed. However, this method uses the watershed algorithm to determine the threshold value to separate the fluids and pores, and the final result is very sensitive to the selection of threshold values; the reliability of the research conclusion remains to be verified [26]. In addition, the existing experimental equipment capable of micro-CT scanning coupled with core flooding tests cannot meet the scanning resolution requirements of low-permeability core. Micromodel is another effective way to visualize the actions between fluids and rock [27, 28]. Bartels et al. [29] intuitively showed the influence of clay minerals on the wettability of the formation through a micromodel modified by clay minerals. Sharifipour et al. [30] visualized the permeability loss caused by clay mineral migration and expansion using a microfluidic model. However, the microfluidic model fails to simulate the mechanisms of formation damage caused by particle migration due to the simple pore structure of the micromodel [31, 32]. Currently, nuclear magnetic resonance (NMR) [33, 34] and Quantitative Evaluation of Minerals by SCANning (QEMSCAN) [35] are capable of accurately characterizing the pore structure and mineral migration during core flooding tests. Fang et al. [36] established a set of core flooding coupled with NMR scans and made quantitative analysis of pore structure change during alkali flooding by utilizing the advantages of NMR in nondestructive detection of pore structure of low-permeability core with the high identification accuracy. Therefore, NMR analysis of cores before and after water flooding can also be used to determine the effects of water flooding on the pore structure of cores. QEMSCAN is an automatic mineralogical identification method combining high-resolution SEM, XRD, and database

technology [37], which scans and identifies minerals in core sections. Zhao et al. [35] used QEMSCAN to study the migration of clay minerals before and after water flooding and its effects on pore structures.

Based on the above research, the paper proposed an integrated experimental method, which can not only quantitatively evaluate the changes of pore throat structure during water injection in a low permeability reservoir but also reveals the mechanisms of permeability loss at the pore scale. The NMR, high-pressure mercury injection (HPMIP), XRD, and SEM were integrated into the core displacement experiment to ensure the accuracy of the experimental results, of which NMR and HPMIP were used to quantitatively evaluate the changes of pore structure before and after water injection, while XRD and SEM were used to analyze the dynamic changes of clay minerals before and after water flooding.

2. Experimental

2.1. Cores. The cores involved in this study were sampled from Chang VIII formation of Ordos Basin in western China. The Chang VIII formation is undergoing a WF since 2011, resulting in some property changes to its ultralow-permeability sandstones physically. The geological properties of the formation are listed in Table 1. From the pore-scale perspective, the rock matrix was composed of quartz, K-feldspar, plagioclase, feldspar, and clays, among which the intergranular-type pores were formed. For another, the pore-size distribution presented two typical types, i.e., unimodal and bimodal. Aiming at a rigorous study, two cores differing in pore size distribution (C9 unimodal and C11 bimodal, respectively) but being on the same permeability level were sampled from a fresh well whose vicinity rocks were never exposed to water, avoiding the subsurface water flush to the rocks. The connate fluids within the cores were extracted by inorganic salts and hydrocarbons, after which the cores were dried in a thermotank under 55°C until reaching stable core weight.

After sampling, both the homogeneous cores were cut into dual parts vertically for direct comparison between the states of the core before-LTWF and after-LTWF (see Figure 1). Accordingly, the four new subcores were named C9-1, C9-2, C11-1, and C11-2. The four subcores were cleaned and dried again to remove the movable fines produced during the cutting process. After that, the four cores were saturated by evacuating and then admitting the deaerated simulated connate water. The core permeability was calculated by Darcy's law after performing the standard flow experiment. Besides, the core porosity was evaluated by the weight-difference method. The permeability and porosity of the cores are listed in Table 2. It shows that the permeability and porosity of dual subcores are almost the same, providing favorable conditions for comparison. Besides, C9 and C11 are on the same property levels although they present different pore-size distributions. The four cores were involved in different tests (see Section 2.3).

2.2. Fluids. The flooding fluid in this study was simulated connate water prepared by reagent grade chemicals corresponding to the ionic components (see Table 3). The total salinity of the water was 25261 ppm, which was on a medium level. Besides, the water is neutral with a pH of 6.89.

Table 1: Geological properties of the Chang VIII formation.

Property	Value	Unit
Depth	1450	m
Thickness	10-20	m
Average porosity	10.2	%
Average permeability	0.35	m
Pore pressure	6.51	MPa
Overburden pressure	12.5	MPa
Reservoir temperature	56.64	°C
Water salinity	25395	ppm

2.3. Procedure. The experiments in this study consisted of preexperiment, formal experiments, and postexperiments operated on C9-1/C11-1, C9-2/C11-2, and C9-2/C11-2, respectively. The experiments on C9 were performed first, and the same ones were repeated on C11. The following descriptions then take C9 as an example.

2.3.1. Preexperiment. The preexperiment involved four tests performed on C9-1. The tests started with splitting the C9-1 into two parts, where part II was a slice with a thickness of 1 cm and part I was the rest (see Figure 1).

The tests operated on part II consisted of the SEM test and XRD test to acquire the pore structure images and mineral proportions, respectively. The SEM test was performed on a piece that was cut from part II and coated with a thin carbon layer, where the coating ensured a clear scanning image. The XRD test was conducted on the rest of part II by using the multifunction X-ray diffractometer (Rigaku TTRIII, Japan).

The NMR test and HPMIP test were performed on part I sequentially. The NMR test was performed using the NMR analyzer (SPEC-RC1). According to the NMR principle, the T_2 spectrum can reflect the pore size distribution. The x-value of the T_2 spectrum, namely, the relaxation time, increased with the pore radius, while the y-value representing the signal amplitude increased with the total pore volume under a specific radius. However, it is required to scale the T_2 spectrum to obtain the real pore-size distribution curve. Hereby, the HPMIP curve was selected as the reference. The HPMIP test was carried out by an automatic mercury intrusion meter (AutoPore IV 9505, USA) allowing a maximum injection pressure of 200 MPa. During the injection, the capillary pressure between mercury and air was as follows:

$$P_c = \frac{2\sigma \cos\theta}{r}, \tag{1}$$

where P_c denotes the capillary pressure, σ denotes the surface tension between mercury and air (480 dyn/cm), θ was the wetting angle between mercury and rock (140°C), and r was

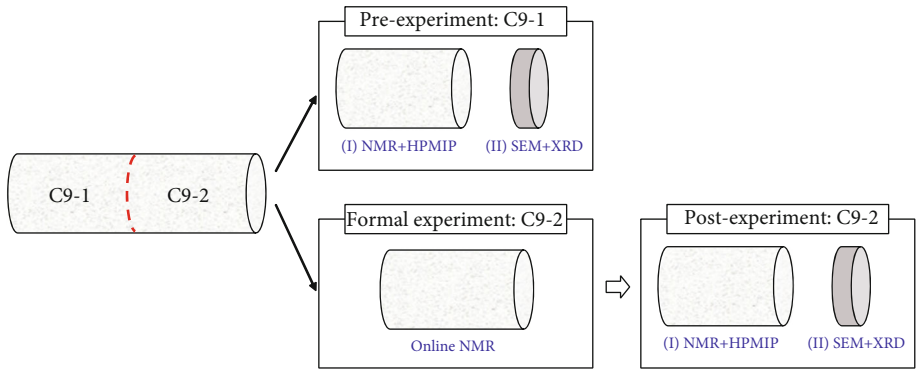

Figure 1: Illustration of the cores and slices.

Table 2: Basic core information.

Cores	Length (cm)	Diameter (cm)	Permeability (mD)	Porosity (%)
C9-1	3.01	2.51	0.362	10.37
C9-2	3.04	2.51	0.365	10.42
C11-1	3.09	2.51	0.374	10.79
C11-2	3.07	2.51	0.378	10.84

Table 3: Ionic components of connate water.

Ion	$Na^+ + K^+$	Ca^{2+}	Mg^{2+}	$Ba^{2+} + Sr^{2+}$	Cl^-	SO_2^{2-}	HCO_3^-
Salinity (ppm)	8738	551	243	172	13888	1465	204

the pore radius. According to the mercury volumes injected into the pores under varying capillary pressures, the real pore-size distribution curve can be obtained. The relaxation time in the T_2 spectrum can be transformed to the pore radius through the linear scaling:

$$T_2 = C \bullet r, \tag{2}$$

where C is the scaling coefficient. C was calculated by fitting the cumulative frequency curves. The T_2 cumulative frequency curve was constructed from the part of the T_2 data conforming to the segment of mercury saturation, and the real cumulative frequency curve was obtained by the HPMIP data.

2.3.2. Formal Experiment. In the formal experiment, the online NMR test was performed in conjunction with the core flow experiment. Differing from the standard flow experiment, the core holder was made of fiberglass to eliminate the magnetic effect of the traditional metallic core holder. For another, the core holder was placed inside the magnetic body of the online NMR system. The experimental setup is shown in Figure 2.

Before the experiment, the C9-2 saturated by simulated connate water was pushed into the core holder, after which the fluorine oil was pumped into the annular space of the holder manually to impose the confining pressure without signal interference of hydrogen on the NMR test.

During the experiment, the water flowed through the core continuously at a stable flux of 0.01 mL/min provided by the ISCO pump (Isco 260D). Meanwhile, the online NMR tests were conducted along with the flooding process simultaneously, which enabled the in situ pore-size evaluations. The entire flowing process lasted for a period of 600 PV to simulate the LTWF. The experimental temperature was controlled at 56°C.The upstream pressure and the NMR T_2 spectrum were recorded at the flooding time of 0 PV, 200 PV, 400 PV, and 600 PV to evaluate the changes of permeability and pore size distribution in the LTWF process.

2.3.3. Postexperiment. In the postexperiment, the operations and four tests of the preexperiment were repeated on C9-2 that has experienced a formal experiment, i.e., the LTWF of 600 PV (see Figure 2). Combining the testing results of pre- and postexperiment, the change of pores and minerals after the LTWF could be evaluated both qualitatively and quantitatively.

3. Results

3.1. Permeability and Porosity. During the water flooding experiment, the permeability and porosity of the core can be calculated using the differential pressure and the total signal amplitude of the T_2 spectrum, respectively. The results are shown in Table 4.

Herein, two indices were used to evaluate the variations of permeability and porosity during the LTWF process:

$$I_k = \frac{k - k_i}{k_i} \times 100\%, I_\varphi = \frac{\varphi - \varphi_i}{\varphi_i}, \tag{3}$$

where I_k denotes the permeability index, I_φ denoted the porosity index, k_i was the initial permeability, and φ_i was the initial porosity. The indices at four LTWF stages are plotted in Figure 3.

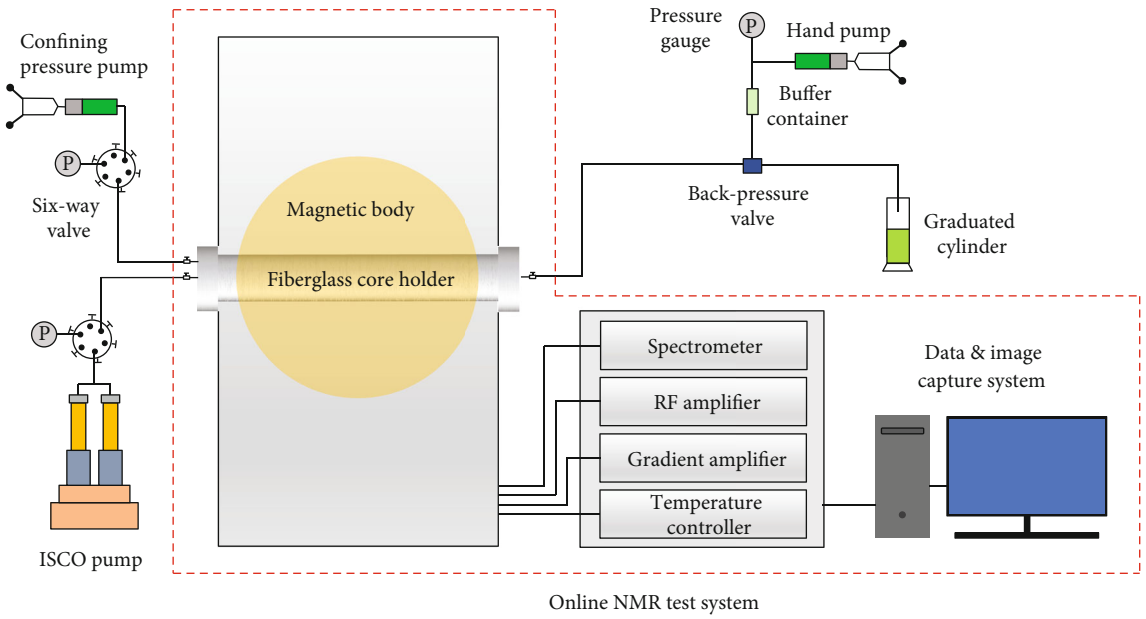

Figure 2: Setup for the formal experiments.

Table 4: Permeability and porosity information.

Cores	Water flooding stage (PV)	Injection pressure (MPa)	Permeability (mD)	Total signal amplitude	Porosity (%)
C9-2	0	0.12805	0.365	1407.48	10.42
	200	0.12951	0.347	1410.18	10.44
	400	0.12994	0.342	1422.34	10.53
	600	0.13003	0.341	1426.39	10.56
C11-2	0	0.12736	0.378	1528.85	10.84
	200	0.13115	0.332	1531.67	10.86
	400	0.13325	0.311	1537.31	10.90
	600	0.13347	0.309	1540.13	10.92

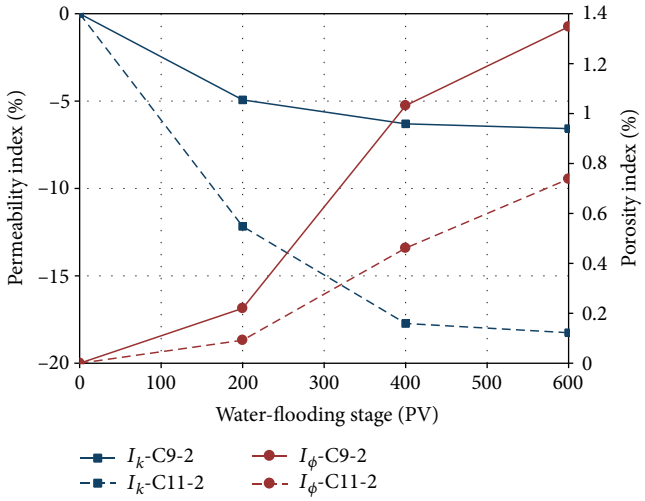

Figure 3: Permeability index and porosity index during the LTWF.

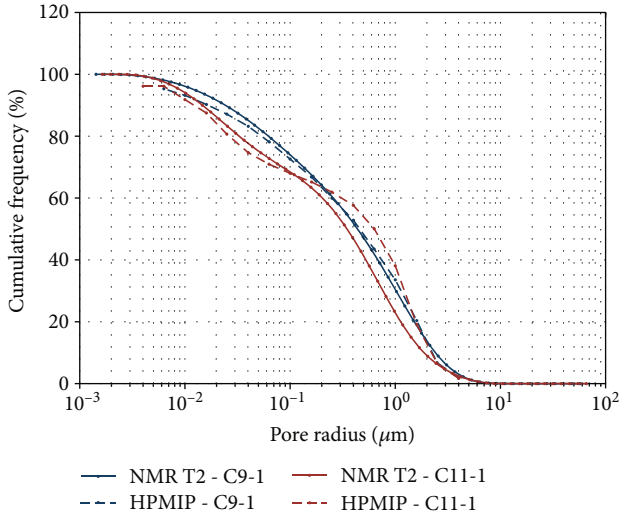

Figure 4: The fitting of cumulative frequency curves.

According to Figure 3, the negative/positive index was observed for the permeability/porosity of both cores, indicating the decrease of permeability and the increase of porosity during the LTWF. Such phenomena were tallied with conventional wisdom from previous studies. The permeability dropped significantly before 400 PV but slightly in 400 PV~600 PV. As for the porosity, the most increment occurred in 200 PV~600 PV. For another, C9-2 showed higher responses to LTWF than C11-2 in terms of permeability, but lower responses in terms of porosity. Specifically, the relative permeability loss of C9-2 and C11-2 at the end of the LTWF was 6.57% and 18.3%, respectively. For the porosity, the maximum relative increment was 1.34% and 0.74%, respectively.

3.2. Pore-Size Distribution. The changes of pore size distribution were evaluated by the T_2 spectrum in the formal

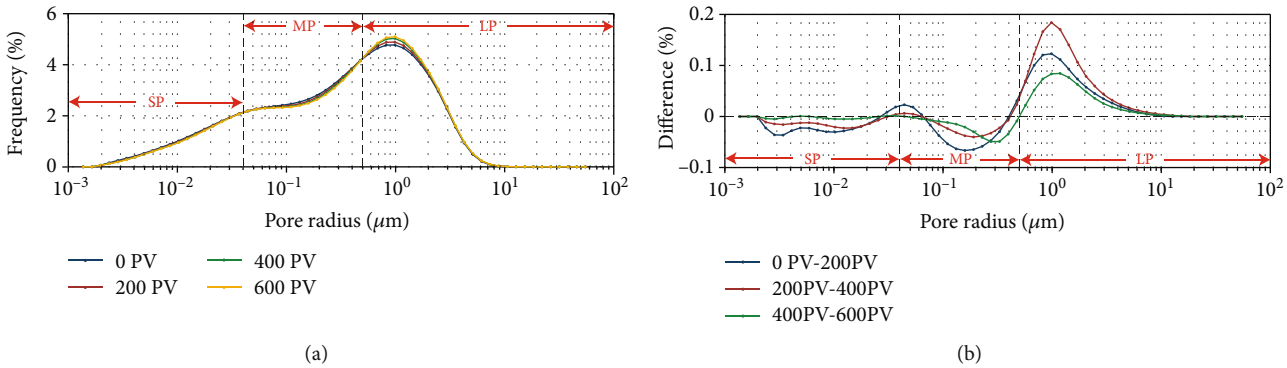

Figure 5: (a) Curves of pore-size distribution of C9-2 at four LTWF stages and (b) differences between adjacent distribution curves.

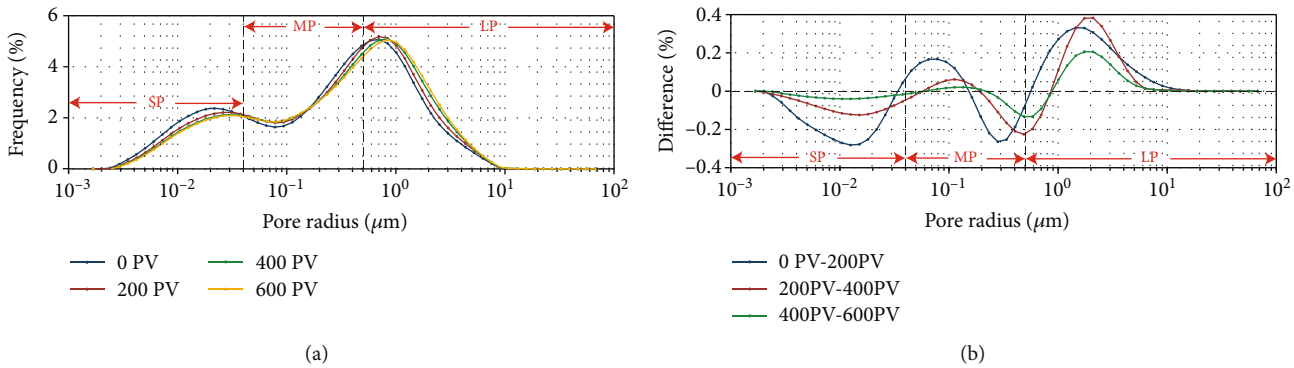

Figure 6: (a) Curves of pore-size distribution of C11-2 at four LTWF stages and (b) differences between adjacent distribution curves.

experiment. As stated in Section 2.3.1, the linear scaling coefficient C was calculated by fitting the cumulative frequency curves. The curves are plotted in Figure 4, which showed good agreement between the T_2 and real cumulative frequency curves for both cores. The least squares regression method was adopted, where the C of C9 and C of C11 were 70.12 and 61.17, respectively.

Figure 5(a) illustrates the curves of the pore-size distribution of C9-2 at four sequential LTWF stages. It showed that the curves of C9-2 presented typical unimodal shapes. Along the LTWF process, the radius of the mainstream pores accounting for the highest proportion remained unchanged, while the peak proportion increased. Figure 5(b) gives the differences between adjacent curves in Figure 5(a). Specifically, the pore could be divided into three levels, i.e., small pores (SPs, $\leq 0.04\,\mu$m), medium pores (MPs, $0.04\,\mu$m~$0.5\,\mu$m), and large pores (LPs, $\geq 0.5\,\mu$m). Accordingly, different levels of pores presented different changing features. The SPs decreased significantly at the early stage (0 PV~200 PV), but the decrement became smaller as the LTWF proceeded. A similar decreasing phenomenon occurred for the MPs except for some increases at the two ends of MPs. For the LPs, there was an obvious increase in the whole LTWF process, where the largest increment occurred around the mainstream pore. The increment of LPs was larger than the decrements of SPs and MPs, and with respect to the stage, the increment was largest at the middle stage (200 PV~400 PV), then early stage and late stage (400 PV~600 PV).

Figure 6(a) illustrates the curves of the pore-size distribution of C11-2 at four stages. The curves of C11-2 presented typical bimodal shapes, where the larger mainstream pores accounted for a higher proportion than the smaller one. Along the LTWF process, the curve shifted to the right, and the radius of mainstream pores increased. Besides, the proportion of smaller mainstream pores decreased, while that of the larger mainstream pores was almost unchanged. Figure 6(b) gives the differences between adjacent curves in Figure 6(a). It showed that the differences of C11-2 were larger than those of C9-2 in all three pore levels. Besides, the differences between the three pore levels were quite near. The SPs decreased, where the largest decrement occurred around the smaller mainstream pore. The smaller MPs increased and the larger ones decreased. For the LPs, the largest increment occurred around the larger mainstream pore. With respect to stage, similarly with C9-2, the decrement of MPs became smaller with stage, and the increment of LPs was largest at the middle stage.

3.3. Characteristic Parameters of Pores. The HPMIP curves at the initial state and after-LTWF state are plotted in Figure 7. It showed that the changes of pore-size distributions in HPMIP curves were consistent with those in NMR T_2 spectra. Table 5 gives the characteristic parameters extracted from HPMIP curves. Similar changing phenomena were observed for C9 and C11. The increase in the average pore radius as well as the median pore radius reflected the expansion of the overall flowing channels, further causing the

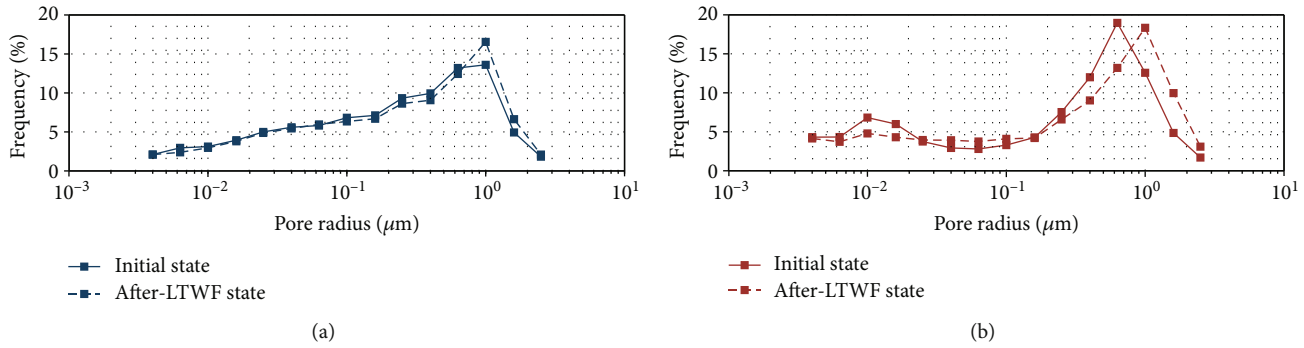

Figure 7: Comparison of the HPMIP curves between the initial state and after-LTWF state: (a) C9 and (b) C11.

Table 5: Comparison of characteristic parameters between the initial state and after-LTWF state.

Cores	C9-1	C9-2	Change (%)	C11-1	C11-2	Change (%)
Type	Unimodality		/	Bimodality		/
State	Initial	After	/	Initial	After	/
Average pore radius (μm)	0.54	0.599	10.93	0.532	0.675	26.73
Median pore radius (μm)	0.296	0.344	16.22	0.402	0.492	22.52
Mainstream pore radius (μm)	1	1	0	0.63	1	58.73
Proportion of mainstream pore (%)	13.607	16.547	21.61	18.97	18.337	-3.34
Structural coefficient	11.553	14.164	22.6	12.045	19.345	60.6
Tortuosity	3.399	3.764	10.72	3.471	4.398	26.73
Relative sorting coefficient	5.476	4.794	-12.45	5.619	4.404	-21.62
Kurtosis	0.882	0.896	1.59	0.687	0.771	12.17

permeability increment. Additionally, the LPs accounted for higher proportions according to the decrease of the relative sorting coefficient. The increases in structural coefficient and tortuosity indicated more tortuous flowing channels. Figure 8 gives the permeability contributions under different pore radii. It showed that the dominated flow channels of both cores were pores with larger radii.

With respect to the comparisons between the two cores, the relative changes showed significant differences. The structural coefficients (C9-11.553, C11-12.045) and tortuosity (C9-3.399, C11-3.471) of the two cores were quite close at the initial state. However, the relative changes of the two parameters for C9 (60.60% and 26.73%) were much larger than those for C11 (22.60% and 10.72%). Moreover, the pore size distribution and permeability contribution of C11 changed more drastically, and its bimodal characteristics became less obvious. In essence, the C9 with unimodality has a more stable pore mechanical structure than C11 with bimodality.

3.4. Clays. Table 6 gives the matrix minerals and clays obtained by the XRD test. The minerals constituting the rock matrix accounted for 83%~84% of the overall minerals. The majority of the matrix minerals were quartz and plagioclase. After LTWF, the matrix minerals were almost unchanged (relative changes: C9-0.48%, C11-0.36%). The clays accounted for 16%~17% of the overall minerals, the majority of which was chlorite. After LTWF, the content of chlorite increased and the contents of the illite/smectite mixed layer and illite/decreased for both C9 and C11.

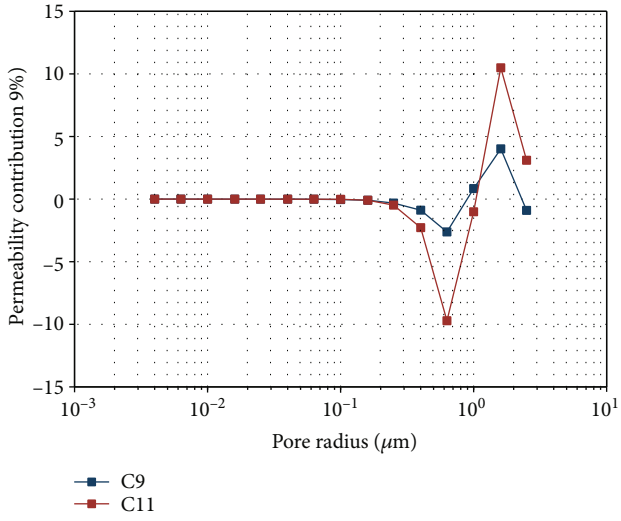

Figure 8: The plot of permeability contribution versus pore radius.

Figure 9 shows the SEM images at the initial state and after-LTWF state. It was observed that the chlorite was filled in the pores with a pompom-like shape (see Figure 9(a)) or attached to the pore walls with a liner-like shape (see Figure 9(d)). The chlorite was brittle mechanically and would break under LTWF, further migrated downstream as fines (see Figures 9(e) and 9(f)). The chlorite filled in the pores partitioned the LPs into several MPs or LPs, increasing flow resistance. In addition,

Table 6: Comparison of matrix minerals and clays between initial state and after-LTWF state.

Core		C9-1	C9-2	C11-1	C11-2
Type		Unimodality		Bimodality	
State		Initial	After	Initial	After
Matrix minerals (%)	Quartz	36.2	36.6	32.5	32.8
	K-feldspar	5.7	6	9.4	9.6
	Plagioclase	41.1	40.9	40.2	39.8
	Calcite	0.7	0.6	0.9	1.1
	Total	83.7	84.1	83	83.3
Clays (%)	Illite/smectite mixed layer	2.8	2.4	2	1.8
	Illite	2.3	1.7	1.7	1.5
	Chlorite	11.2	11.8	13.3	13.4
	Total	16.3	15.9	17	16.7

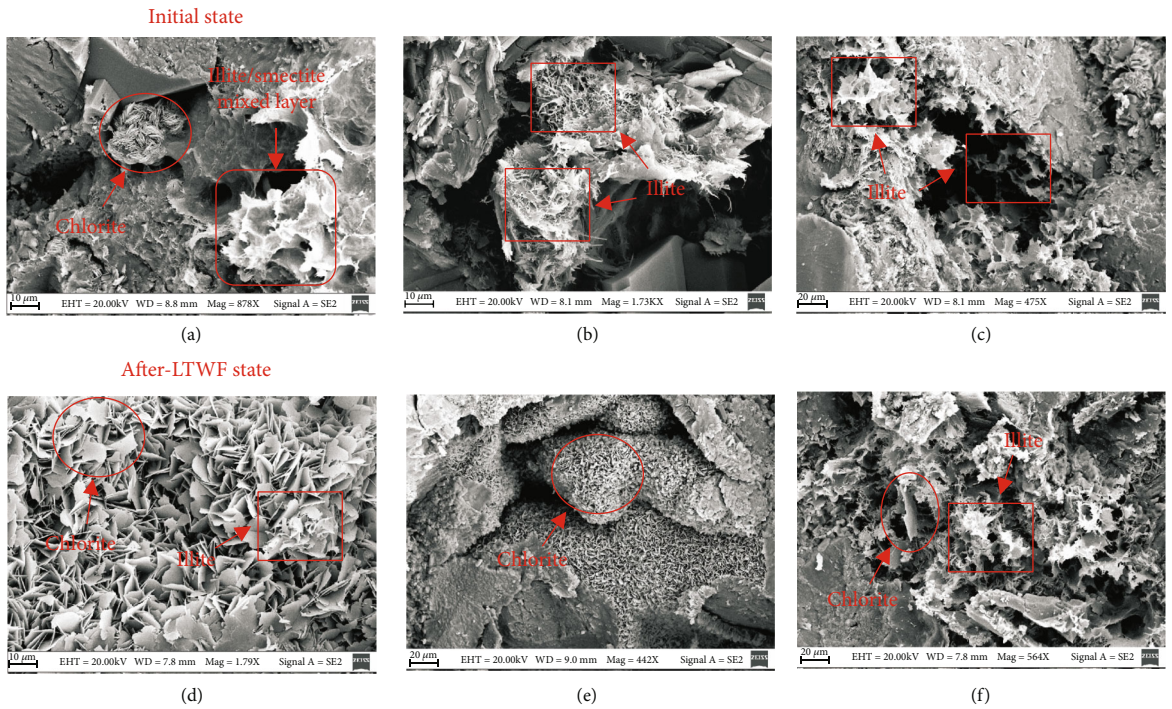

Figure 9: The SEM images at the initial state and after-LTWF state.

such chlorites may hinder the migration of fines and cause their blockage. The chlorites attached to the pore walls caused higher roughness of the pore walls, and therefore, the migratory fines may be trapped and the pore radius decreased (see Figures 9(d) and 9(e)).

The illite formed a bridge in the pores with the strand-like shape or feather-like shape, leading to an increase of tortuosity and the blockage of large migratory fines (see Figure 9(f)). Additionally, the illite may form smaller migratory fines after LTWF, which flows downstream with the fluid more smoothly.

The illite/smectite mixed layer existed with the honeycomb-like shape (see Figure 9(a)). Such clays had more smooth surfaces, and the smaller migratory fines were trapped in small probability. However, the blockage of larger migratory fines would occur.

4. Discussion

4.1. Mechanism of Property Changes in LTWF. According to the experimental results of both cores, microscopically, the clays changed physically during the LTWF, which further resulted in the changes of pore structure. Consequently, macroscopic property changes occurred, i.e., permeability, porosity, pore size distribution, and characteristic parameters. The clays can induce changes in pore structure in two possible ways: swelling and migration. The two cores in this paper were essentially free of swelling clay (Table 6), and the simulated water had the same salinity as connate water. Therefore, the changes in pore structures were induced by clay migration in this paper. As the properties changed differently at the three LTWF stages, the physical processes at the three stages were interpreted as follows.

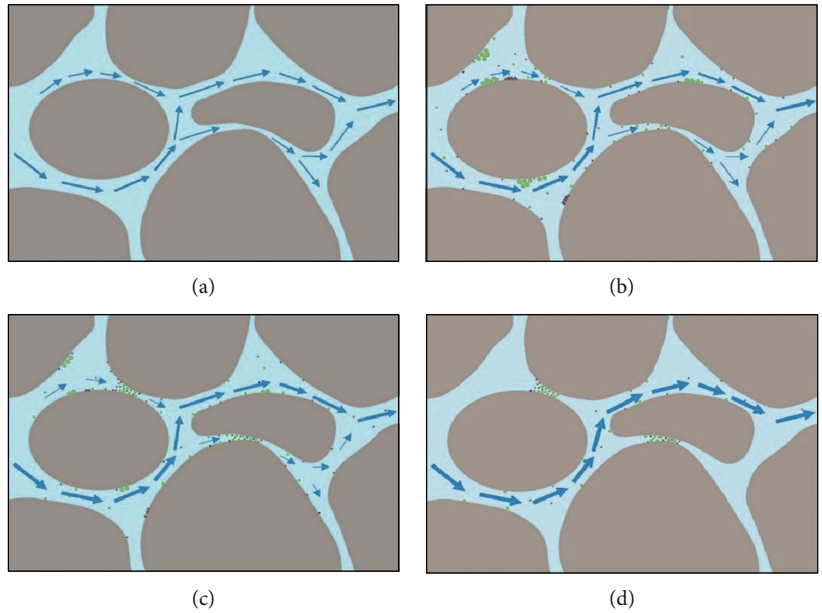

Figure 10: Illustration of the pore structure at different stages: (a) initial state, (b) early stage, (c) middle stage, and (d) late stage.

At the initial stage, the pores were connected by throats of different sizes, forming multiple microscopic channels with different flow capacities (see Figure 10(a)). At the early stage, the clay released from the pores as the water flushed through the channels continuously, and consequently, the movable particles formed. The phenomenon of significant changes of pore size distribution indicated that the released particles have redistributed. Specifically, the blockage occurred in SPs due to the small spatial channels and weak flow capacity, which resulted in the reduction of SPs (see Figure 10(b)). For MPs and LPs, the released particles migrated downstream. The pores where the particles released became larger, while the pores where the particles accumulated became smaller (see Figure 10(b)). Additionally, the effluxes of particles were rare at this stage according to small changes of porosity.

At the middle stage, the decrements of SPs and permeability became smaller, which indicated that the blockage induced by the released particles weakened. Besides, the changes of permeability contribution showed that some flow channels formed by MPs and LPs became dominant flow channels gradually (see Figure 10(c)). The dominant flow channels accepted more fluid flows, and therefore, the flushes in such channels were severer. Additionally, the effluxes of particles occurred at this stage according to a significant increase of porosity.

At the late stage, the phenomenon of unchanged SPs and permeability revealed that the stable flow channels have formed (see Figure 10(d)). However, some changes still existed, i.e., decreasing MPs, increasing LPs, and slightly increasing porosity. Such changes showed that the processes of migration and efflux still existed but to a small extent.

4.2. Difference between Unimodal Core and Bimodal Core. The comparison of experimental results between the unimodal core (C9) and bimodal core (C11) showed that the property changes of the bimodal core were more obvious than those of the unimodal core. Specifically, the blockages in MPs of the bimodal core were severer, resulting in a larger decrease of MPs, a larger increase of tortuosity, and a larger decrease of permeability. For another, the more significant changes of MPs and LPs and the shifts of curve peaks demonstrated that the migration and accumulation of particles were severer. Such phenomena of the bimodal core induce larger changes of permeability contribution. In general, the pore structures as well as the macroscopic properties of the bimodal core were more unstable, which led to a higher response to the LTWF.

The different responses of the two types of cores could be essentially attributed to the content differences of clay between the two cores. After LTWF, the contents of the illite and illite/smectite mixed layer increased, while the contents of chlorite increased. Such changes resulted from the microscopic morphologies of the three clays. According to SEM images, the illite and illite/smectite mixed layers were more easily to release and to form tiny movable particles which migrated downstream and outflow. The chlorite with a scaly shape was less likely to migrate to faraway places. The changes of pore structure were dominated by chlorite due to its highest proportion. The bimodal core had more chlorite than the unimodal core at the initial state. Therefore, the more significant changes of pore structure, pore size distribution, and permeability occurred in the bimodal core because of the migration and accumulation caused by chlorite. In contrast, the main physical processes of the unimodal core were the blockage by tiny particles and efflux, and therefore, the unimodal core showed a lower response to the water flush.

5. Conclusions

This paper provided comprehensive insights into the LTWF by performing standard core flow experiments in conjunction with a couple of tests consisting of online NMR, HPMP,

XRD, and SEM. Both the unimodal core and bimodal core were involved in the study. The main contributions were outlined as follows.

LTWF caused a decrease of permeability and the increase of porosity. The unimodal core showed higher responses to LTWF than the bimodal core in terms of permeability, but lower responses in terms of porosity.

(1) As the LTWF proceeded, the SPs decreased and the LPs increased for both cores. For the unimodal core, the radius of the mainstream pores remained unchanged, while the peak proportion increased. For the unimodal core, the pore-size distribution curve shifted to the right, and the radius of mainstream pores increased. The proportion of smaller mainstream pores decreased, while that of the larger mainstream pores was almost unchanged

(2) After LTWF, the average pore radius, median pore radius, structural coefficient, and tortuosity increased, while the relative sorting coefficient decreased. The relative changes of the parameters for the unimodal core were much smaller than those for the bimodal core

(3) The clays in both cores consisted of chlorite, illite/smectite mixed layer, and illite, the majority of which was chlorite. After LTWF, the content of chlorite increased and the contents of the illite/smectite mixed layer and illite decreased

(4) During the process of LTWF, fines such as chlorite, illite/smectite mixed layer, and illite detached from the pore surface and transported in pore throats. When the fines get stuck in SPs, core structure coefficient and tortuosity will increase, which accordingly reduce the flow capacity of connected pores. The change of MPs and LPs structure is mainly caused by detachment and loss of chlorite, which makes the average and median pore radius bigger

(5) The changes of pore structure and macroscopic properties were induced by the clays. At the early stage, the blockage of the released clays occurred in SPs. Some of the MPs and LPs became larger due to the release and some of them became smaller due to the accumulation. At the middle stage, the blockage of SPs weakened. Some flow channels formed by MPs and LPs became dominant flow channels gradually. The effluxes of particles occurred, resulting in a significant increase in porosity. At the late stage, the stable flow channels have formed. Some changes still existed due to migration and efflux but to a small extent

(6) The higher response of the bimodal core to LTWF could be attributed to its higher content of chlorite. The chlorite with a scaly shape was less likely to migrate to faraway places, and therefore, the released chlorite accumulated, which caused significant changes of pore structure

Data Availability

The data used to support the findings of this study are available from the corresponding author upon request.

Conflicts of Interest

The authors declare no conflicts of interest.

Authors' Contributions

Conceptualization was done by Hanqiao Jiang and Shiyuan Qu; the experimental design was done by Junjian Li; experiments were done by Shiyuan Qu and Changhui Wu; writing the original draft preparation was done by Shiyuan Qu; writing the review and editing were done by Lin Zhao.

Acknowledgments

This research was supported by the Major Program of the National Natural Science Foundation of China (Grant ID: 2017ZX05009-005), the Strategic Consulting Project of Chinese Academy of Engineering Physics (Grant ID: 2018-XZ-09), and the National Key Basic Research Development Plan (Grant ID: 2015CB250905).

References

[1] W. G. Anderson, "Wettability literature survey-part 6: the effects of wettability on waterflooding," *Journal of Petroleum Technology*, vol. 39, no. 12, pp. 1605–1622, 1987.

[2] M. Dong and I. Chatzis, "The imbibition and flow of a wetting liquid along the corners of a square capillary tube," *Journal of Colloid and Interface Science*, vol. 172, no. 2, pp. 278–288, 1995.

[3] P. Kasza, M. Czupski, K. Wilk, M. Masłowski, R. Moska, and Ł. Leśniak, "Laboratory testing of novel polyfraction nanoemulsion for EOR processes in carbonate formations," *Energies*, vol. 13, no. 16, p. 4175, 2020.

[4] B. Yuan and D. A. Wood, "A holistic review of geosystem damage during unconventional oil, gas and geothermal energy recovery," *Fuel*, vol. 227, pp. 99–110, 2018.

[5] M. Ali, H. H. Jarni, A. Aftab et al., "Nanomaterial-based drilling gluids for exploitation of unconventional reservoirs: a review," *Energies*, vol. 13, no. 13, article 3417, 2020.

[6] M. Zhao, M. Cao, H. He, and C. Dai, "Study on variation laws of fluid threshold pressure gradient in low permeable reservoir," *Energies*, vol. 13, no. 14, article 3704, 2020.

[7] L. Wilson, M. J. Wilson, J. Green, and I. Patey, "The influence of clay mineralogy on formation damage in North Sea reservoir sandstones: a review with illustrative examples," *Earth-Science Reviews*, vol. 134, pp. 70–80, 2014.

[8] C. G. Li and S. Y. Xu, "Law of pore structure variety in reservoir during a long episode waterflooded development," *Petroleum Exploration and Development*, vol. 30, no. 2, pp. 94–96, 2003.

[9] Q. Du, "Variation law and microscopic mechanism of permeability in sandstone reservoir during long-term water flooding development," *Acta Petrolei Sinica*, vol. 37, no. 9, pp. 1159–1164, 2016.

[10] Y. B. Lin, J. Zhang, X. G. Liu, and H. T. Zhou, "Pore structure features of reservoirs at late high water-cut stage, Lamadian Oilfield, Daqing, China," *Petroleum Exploration and Development*, vol. 35, no. 2, pp. 215–219, 2008.

[11] C. Shi, F. Zhang, and P. Chen, "Affection of simulating waterflooding by water injectiontests on reservoir properties," *Journal of Southwest Petroleum University*, vol. 35, no. 5, pp. 87–93, 2013.

[12] J. Yu, "New method of experimental research on the influence of long-term water flooding on low reservoir physical properties," *Inner Mongolia Petrochemical Industry*, vol. 43, no. 6, pp. 116–118, 2017.

[13] S. Wu, "Variation rule of oil layer parameters washed by long-term injected water and its impact on development effect," *Petroleum Geology Oilfield Development in Daqing*, vol. 25, no. 4, pp. 35–37, 2006.

[14] W. Q. Jin, X. J. Wang, F. P. He, and T. S. Chen, "Characteristics of chang-6 oil-bearing formation changes after long term waterflood development in Ansai Oilfield," *Journal of Earth Sciences and Environment*, vol. 32, no. 3, pp. 239–244, 2010.

[15] M. Yu, A. Zeinijahromi, P. Bedrikovetsky et al., "Effects of fines migration on oil displacement by low-salinity water," *Journal of Petroleum Science & Engineering*, vol. 175, pp. 665–680, 2019.

[16] K. C. Khilar and H. S. Fogler, "Water sensitivity of sandstones," *Society of Petroleum Engineers Journal*, vol. 23, no. 1, pp. 55–64, 1983.

[17] H. A. Omar, N. I. M. Yusoff, H. Ceylan et al., "Determining the water damage resistance of nano-clay modified bitumens using the indirect tensile strength and surface free energy methods," *Construction & Building Materials*, vol. 167, pp. 391–402, 2018.

[18] S. S. Alian, A. A. Omar, A. F. Alta'ee, and I. Hani, "Study of asphaltene precipitation induced formation damage during CO_2 injection for a Malaysian light oil," *World Academy of Science, Engineering and Technology*, vol. 78, pp. 733–737, 2011.

[19] M. J. Wilson, *Sheet Silicates: Clay Minerals*, Geological Society, 2013.

[20] M. J. Wilson, L. Wilson, and I. . Patey, "The influence of individual clay minerals on formation damage of reservoir sandstones: a critical review with some new insights," *Clay Minerals*, vol. 49, no. 2, pp. 147–164, 2014.

[21] G. Odriozola and F. D. J. Guevara-Rodríguez, "Na-montmorillonite hydrates under basin conditions: hybrid Monte Carlo and molecular dynamics simulations," *Langmuir*, vol. 20, no. 5, pp. 2010–2016, 2004.

[22] S. S. Rahman, M. M. Rahman, and F. A. Khan, "Response of low-permeability, illitic sandstone to drilling and completion fluids," *Journal of Petroleum Science & Engineering*, vol. 12, no. 4, pp. 309–322, 1995.

[23] C. L. G. Amorim, R. T. Lopes, R. C. Barroso et al., "Effect of clay-water interactions on clay swelling by X-ray diffraction," *Nuclear Instruments and Methods in Physics Research Section A: Accelerators, Spectrometers, Detectors and Associated Equipment*, vol. 580, no. 1, pp. 768–770, 2007.

[24] K. Elraies and A. E. A. Basbar, "The effect of water salinity on silica dissolution rate and subsequent formation damage during chemical EOR process," *Journal of Petroleum & Environmental Biotechnology*, vol. 6, no. 2, article 1000209, 2015.

[25] J. Li, H. Jiang, C. Wang et al., "Pore-scale investigation of microscopic remaining oil variation characteristics in water-wet sandstone using CT scanning," *Journal of Natural Gas Science and Engineering*, vol. 48, pp. 36–45, 2017.

[26] F. Yu, H. Jiang, F. Xu et al., "A multi-scale experimental study of hydrophobically-modified polyacrylamide flood and surfactant-polymer flood on enhanced heavy oil recovery," *Journal of Petroleum Science and Engineering*, vol. 182, article 106258, 2019.

[27] F. Yu, H. Jiang, M. Ma, F. Xu, H. Su, and J. Jia, "Visualization the surfactant imbibition at pore scale by using of fractured micromodels," in *SPE Improved Oil Recovery Conference*, Tulsa, 2020.

[28] F. Yu, H. Jiang, Z. Fan, F. Xu, H. Su, and J. Li, "Formation and flow behaviors of in situ emulsions in heavy oil reservoirs," *Energy & Fuels*, vol. 33, no. 7, pp. 5961–5970, 2019.

[29] W. B. B. Bartels, H. Mahani, S. Berg, R. Menezes, J. A. van der Hoeven, and A. Fadili, "Oil configuration under high-salinity and low-salinity conditions at pore scale: a parametric investigation by use of a single-channel micromodel," *SPE Journal*, vol. 22, no. 5, pp. 1362–1373, 2017.

[30] M. Sharifipour, A. Nakhaee, and P. Pourafshary, "Model development of permeability impairment due to clay swelling in porous media using micromodels," *Journal of Petroleum Science & Engineering*, vol. 175, pp. 728–742, 2019.

[31] F. Yu, H. Jiang, F. Xu, Z. Fan, H. Su, and J. Li, "New insights into flow physics in the EOR process based on 2.5D reservoir micromodels," *Journal of Petroleum Science & Engineering*, vol. 181, article 106214, 2019.

[32] F. Yu, H. Jiang, Z. Fan et al., "Features and imbibition mechanisms of Winsor I type surfactant solution in oil-wet porous media," *Petroleum Exploration and Development*, vol. 46, no. 5, pp. 1006–1013, 2019.

[33] M. Wang, J. Xie, F. Guo, Y. Zhou, X. Yang, and Z. Meng, "Determination of NMR T_2 cutoff and CT scanning for pore structure evaluation in mixed siliciclastic–carbonate rocks before and after acidification," *Energies*, vol. 13, no. 6, article 1338, 2020.

[34] T. Zhou, C. Wu, Z. Shi et al., "Multi-scale quantitative characterization of pore distribution networks in tight sandstone by integrating FE-SEM, HPMI, and NMR with the constrained least squares algorithm," *Energies*, vol. 12, no. 18, article 3514, 2019.

[35] L. Zhao, H. Jiang, J. Li, and J. Li, "Pore-scale evaluation on the mechanism of water sensitivity for sandstones containing non-swelling clays," *Arabian Journal of Geosciences*, vol. 13, no. 2, 2020.

[36] W. Fang, H. Jiang, J. Li et al., "A new experimental methodology to investigate formation damage in clay-bearing reservoirs," *Journal of Petroleum Science and Engineering*, vol. 143, pp. 226–234, 2016.

[37] K. Ma, H. Jiang, J. Li, and L. Zhao, "Experimental study on the micro alkali sensitivity damage mechanism in low- permeability reservoirs using QEMSCAN," *Journal of Natural Gas Science and Engineering*, vol. 36, pp. 1004–1017, 2016.